PHYSICAL REVIEW B VOLUME 52, NUMBER 2 1 JULY 1995-II

Subpicosecond time-resolved Raman investigation of optical phonon modes in Cr-doped forsterite

S. G. Demos and R. R. Alfano
Institute for Ultrafast Spectroscopy and Lasers, Center for Advanced Technology for Ultrafast Photonic Materials and Applications, Department of Physics, The City College and Graduate School of the City University of New York, New York, New York 10031

(Received 23 February 1995)

The nonradiative relaxation dynamics of forsterite was investigated by studying different phonon modes using time-resolved Raman spectroscopy. We found that only the 225, 335, and 370 cm^{-1} anti-Stokes Raman lines exhibit changes in their intensity at various pump-probe delay times indicating the presence of nonequilibrium phonon populations. The experiments were performed at room and liquid nitrogen temperatures. A rate equations analysis was used to describe the dynamics of the ion-lattice system. The nonradiative relaxation time and the phonon lifetimes were estimated by fitting to the experimental data.

I. INTRODUCTION

A tunable solid-state laser crystal is composed of a host dielectric crystal doped with small concentrations of an impurity transition-metal ion. Within picoseconds after photoexcitation, an excited ion reaches the lowest vibrational level of the excited state which is a metastable level (storage level) of the system.[1–4] The phonons emitted during this process last for ≈10 ps prior to their break down into low-energy large-wave-vector acoustic phonons that have longer lifetimes and are responsible for the dissipation of the energy into the crystal.[5–7] There are two fundamental questions associated with the nonradiative relaxation: which optical phonon modes participate in the nonradiative decay and what is the ultrafast temporal dynamics of the coupled ion-lattice system following photoexcitation. Recently, utilizing the up-converted hot luminescence technique[8,9] in forsterite, the energy of phonon modes involved in the initial steps of the vibrational relaxation of the photoexcited Cr^{4+} ions were measured. The energy separation between the peaks in the up-converted hot luminescence spectrum indicates that the participating phonons are 218±20, 323±20, 365±20, and 515±15 cm^{-1}. The up-converted hot luminescence spectra show the presence of an electronic bottleneck centered at 2.1 eV. The lifetime of the hot luminescence emission from the bottleneck was measured to be shorter than 10 psec at room and liquid-nitrogen temperatures. In addition, time-resolved Raman-scattering measurements in forsterite have shown that at room temperature the intensity of the 225 and 335 cm^{-1} anti-Stokes Raman lines of the probe beam were changing at various delay times providing the dynamics of nonequilibrium phonons generated during the transfer of energy from the excited Cr^{4+} ions into the surrounding lattice.[10]

In this paper, we report on the results of a time-resolved investigation of different Raman-active phonon modes in Cr^{4+}-doped forsterite at room and liquid-nitrogen temperatures. The objective of this line of research is to advance our knowledge on the nonradiative relaxation processes in tunable solid-state laser crystals. From a number of Raman-active modes that we investigated, only the 225, 335, and 370 cm^{-1} modes exhibited detectable changes in intensity at various pump-probe delay times. The observed nonequilibrium phonon populations are associated with the overall complex nonradiative decay following the excitation of the impurity Cr^{4+} ions. Using rate equations to describe the ion-lattice system, the nonradiative relaxation time, the phonon lifetimes and the electronic bottleneck lifetime were estimated by fitting to the experimental data. The nonradiative relaxation time and the lifetime of the bottleneck are estimated to be in the order of few ps, while the phonon lifetimes are of the order of 10 ps. The fit suggests the presence of an electronic bottleneck immediately after photoexcitation with an estimated lifetime of 3 ps at room temperature.

II. EXPERIMENTAL METHOD

A synchronously pumped Rh-6G dye laser (Spectra Physics, model 3000) tuned at 590 nm was used to photoexcite Cr ions in a Cr-doped forsterite crystal ($Cr:Mg_2SiO_4$) (Refs. 11–14) containing 0.02 at. % of Cr. Forsterite is a member of the olivine family. It has an orthorhombic structure with space group P_{bnm}.[13,14] The unit-cell dimensions are $a = 4.76$ Å, $b = 10.22$ Å, $c = 5.99$ Å and it contains four formula units per unit cell, i.e., 28 atoms. The Mg atoms occupy octahedral sites in two crystallographically distinct position, which have inversion and mirror point symmetry, while the Si atoms occupy tetrahedral sites. Cr^{3+} and Cr^{4+} coexist in forsterite crystals and their relative concentration depends on the growth atmosphere. The tetravalent chromium replaces Si in the Mg_2SiO_4 host in tetrahedral sites. The trivalent chromium substitutes for the octahedrally coordinated Mg ions. The absorption and emission spectral profiles of the sample indicate that the sample contains mostly Cr^{4+} ions.

The modes of vibration of the host Mg_2SiO_4 crystal are separated into internal (SiO_4) and external (lattice) modes.[13,14] In Table I, all the modes observed in the Raman-scattering spectra and in the infrared absorption measurements are provided as they have been given in the literature. The 1050–800 cm^{-1} region corresponds to various stretching vibrations of the SiO_4 tetrahedron; the symmetric stretch modes are denoted as (ν_1), while the antisymmetric stretch modes are denoted as (ν_3).

0163-1829/95/52(2)/987(10)/$06.00

The 650–475 cm^{-1} region corresponds to bending vibrations of the SiO$_4$; twofold and threefold degenerate deformation modes exist in this spectral region and are denoted as (ν_2) and (ν_4), respectively. Below 475 cm^{-1} are the external modes of vibration, which are described as translations of the Mg ions or of the SiO$_4$ along a crystal axis [T_i(Mg) or T_i(SiO$_4$)], or rotations of the SiO$_4$ [R_i(SiO$_4$)].

The 590 nm laser excitation wavelength was selected in order to be as close as possible to the maximum of the absorption peak of the $^3T_1$ electronic state, while the observed anti-Stokes luminescence is at a low level to clearly observe the anti-Stokes Raman lines. The strong anti-Stokes luminescence appears when the temperature of the sample is higher than $T \approx 200$ K and the excitation wavelength is longer than ≈ 595 nm.

The optical configuration is shown in Fig. 1. The output power of the dye laser was ≈ 200 mW operating at a repetition rate of 82 MHz. The laser pulsewidth was 450 fs and it was continuously monitored by an autocorrelator. The spectral width of the laser output was 58 cm^{-1} but it was reduced for better spectral resolution down to

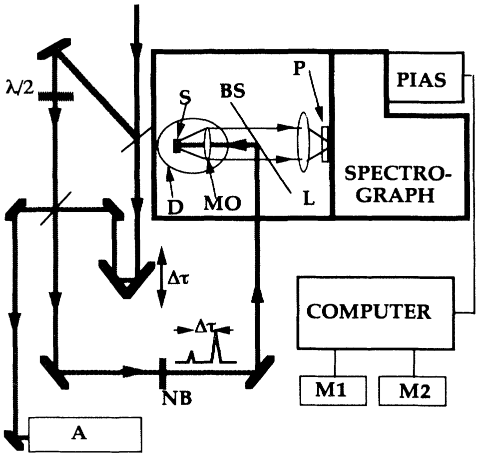

FIG. 1. Time-resolved Raman spectroscopy experimental setup (Δτ: delay time, A: autocorrelator, λ/2: half-wave plate, NB: narrow-band interference filter, D: optical cryostat, S: sample, MO: microscope objective, BS: beam-splitter, L: lens, P: polarizer, M1 and M2: computer monitors 1 and 2).

TABLE I. Lattice vibrational modes of Mg$_2$SiO$_4$ observed in Raman-scattering and infrared absorption spectra and their assignment.

Symmetry	Experiment	Assignment
A_g	966	ν_3
	856	ν_3
Raman	826	ν_1
active	609	ν_4
	546	ν_4
	424	ν_2
	340	$R_c(\mathrm{SiO_4})$
	329	$T_b(\mathrm{MgII})$
	305	$T_a(\mathrm{MgII,\ SiO_4})$
	227	$T_b(\mathrm{SiO_4,\ MgII})$
	183	$T_a(\mathrm{MgII,\ SiO_4})$
B_{2g}	884	ν_3
	588	ν_4
Raman	441	ν_2
active	368	$R_b(\mathrm{SiO_4})$
	324	$R_a(\mathrm{SiO_4})$
	244	$T_c(\mathrm{SiO_4})$
	142	$T_c(\mathrm{MgII})$
B_{1g}	976	ν_3
	866	ν_3
Raman	839	ν_1
active	632	ν_4
	583	ν_4
	434	ν_2
	418	$R_c(\mathrm{SiO_4})$
	318	$T_b(\mathrm{MgII})$
	260	$T_a(\mathrm{MgII,\ SiO_4})$
	224	$T_a(\mathrm{MgII,\ SiO_4})$
	192	$T_b(\mathrm{SiO_4,\ MgII})$
B_{3g}	922	ν_3
	595	ν_4
Raman	412	ν_2
active	376	$R_c(\mathrm{SiO_4})$
	318	$R_b(\mathrm{SiO_4})$
	272	$T_c(\mathrm{MgII})$
	226	$T_c(\mathrm{SiO_4})$

Symmetry	Exper.(TO/LO)	Assignment
B_{1u}	885/994	ν_3
	502/585	ν_4
IR	483/489	ν_2
active	423/459	$R_c(\mathrm{SiO_4})$
	296/318	$T_c(\mathrm{MgI})$
	274/278	$T_b(\mathrm{MgII})+T_c(\mathrm{MgI})$
	224/--	$T_a(\mathrm{MgI})$
	201/--	$T_{b,c}(\mathrm{MgI})$
B_{2u}	987/993	ν_3
	882/979	ν_3
IR	838/843	ν_1
active	537/597	ν_4
	510/516	ν_4
	465/493	ν_2
	421/446	$R_c(\mathrm{SiO_4})$
	400/412	$T_c(\mathrm{MgI})$
	352/376	$T_{b,c}(\mathrm{MgII})$
	294/313	$T_{a,c}(\mathrm{MgI})+T_b(\mathrm{MgII})$
	280/283	$T_b(\mathrm{MgI})$
	224/--	$T_a(\mathrm{MgII})$
	201/--	$T_a(\mathrm{MgI,SiO_4})$
B_{3u}	980/1086	ν_3
	957/963	ν_3
IR	838/845	ν_1
active	601/645	ν_4
	562/566	ν_4
	498/544	ν_2
	403/469	$R_a(\mathrm{SiO_4})$
	378/386	$T_c(\mathrm{MgI})$
	320/323	$T_{b,c}(\mathrm{MgI})$
	293/298	$T_{a,c}(\mathrm{MgI})$
	274/276	$T_a(\mathrm{MgI})+T_b(\mathrm{MgII})$
	224/--	$T_{a,b}(\mathrm{MgII})$
	201/--	$T_b(\mathrm{MgI,SiO_4})$

36 cm^{-1} using a narrow-band interference filter without any observable change in the pulse duration. Each laser pulse is divided in two parts to compose the pump and probe pulses. The probe beam passes through an adjustable optical delay line. The polarization of the pump beam was rotated by 90° using a half-wave plate. Zero delay at the position of the sample was determined to within ±150 fs by mixing of the pump with the probe beams in a thin KDP (KH_2PO_4) crystal and monitoring the second harmonic signal. The pump and probe excitation beams are focused and the backscattered light is collected by a (10×) microscope objective lens. The effective focal length of this lens is ≈ 1 cm and therefore, the spot diameter of the laser beam in the focal point is estimated to be in the range of 10 μm. For the low-temperature measurements, the microscope objective was positioned inside the optical cryostat. At low temperatures, the index matching material positioned between individual lenses composing the microscope objective breaks into very small pieces and the lens loses its transparency. For this reason, the lenses were taken apart and the index matching material was removed for safe use at liquid-nitrogen temperature. The modified lens is backscattering a portion of the incident laser beam. This causes increased background noise in our measurements and as result, the error bar for these measurements is increased.

The pump and probe beams are cross polarized with respect to the crystal axis resulting in a different set of Raman lines from each beam.[13,14] The intensity of the lines arising from the preceding pump pulses is independent of the pump-probe delay time and it depends only on the average laser power. On the other hand, the Raman lines arising from the probe pulses are monitoring the average phonon population of the respective phonon modes for possible delay-time-dependent changes in their intensity. Changes in the intensity of the probe beam associated Raman lines indicate the presence of nonequilibrium phonon populations generated during the nonradiative decay following the photoexcitation of the Cr ions by the pump pulse. For negative delay times, the probe pulses arrives before the pump pulses and nonequilibrium phonons can be generated by the probe pulse that can cause an increase of the intensity of the pump Raman lines. Therefore, the pump Raman lines can be used as a reference indicating the average laser beam output only for positive delay times.

The detection system is composed by a SPEX triplemate spectrograph and an ultrasensitive photon-counting image acquisition system (PIAS, Hamamatsu, model C1815). Using the pump-beam Raman lines as reference, the change in the phonon population is monitored from the ratio of the intensities of the probe associated Raman lines over the reference Raman line of the pump. The ratio is obtained using the integrated peak intensities over a spectral width of 26 cm^{-1} after subtraction of the luminescence background. This method is particularly efficient when small changes must be observed while the laser output power is fluctuating in time. The ratio of the pump- and probe-beam intensities remains the same and therefore, changes in the relative intensity of the Raman lines is independent from the fluctuations of the laser power reflecting only changes in the phonon population.

The experiments were performed for different pump-probe-scattered light polarization configurations with respect to the crystal axis. Due to the selection rules, the possible polarization combinations that allow the study of most of the Raman phonon modes observed in the backscattering geometry are limited to three configurations. Excitation with laser polarization parallel to the c axis of the crystal was preferable due to the stronger absorption exhibited by the Cr^{4+} ions at the 590 nm excitation wavelength.

In the first configuration, the pump-beam polarization (P_{pump}) is parallel to the c axis, the probe-beam polarization (P_{probe}) parallel to the b axis and the collected backscattered light polarization (P_{scatt}) parallel to the b axis of the crystal. in this case, the 225, 335, 545, and 826 cm^{-1} Raman lines are due to the probe beam and can be investigated for possible time-dependent changes in intensity. The second configuration is $P_{\mathrm{pump}} \| c$, $P_{\mathrm{probe}} \| b$, and $P_{\mathrm{scatt}} \| c$ axis of the crystal. The Raman lines due to the probe beam are at 370, 590, and 884 cm^{-1}. The third configuration is $P_{\mathrm{pump}} \| c$, $P_{\mathrm{probe}} \| a$, and $P_{\mathrm{scatt}} \| a$ axis. The probe-beam Raman lines examined in this case are the 300, 502, 609, 770, 826, and 856 cm^{-1} modes. The power of the pump and probe laser beams used for each polarization configuration was chosen to generate Raman lines of approximately the same intensity. For this reason, the ratio of the pump-beam power over the probe-beam power for the first and third configuration was chosen to be 3/1, while for the second configuration the ratio was 1/1.

Using these three scattering configurations, we investigated the 225, 300, 335, 370, 502, 545, 590, 609, 770, 826, 856, and 884 cm^{-1} modes at room temperature for possible changes in their intensity as a function of the pump-probe time delay. We found that only the 225, 335, and 370 cm^{-1} modes exhibited detectable changes in their intensity. The temporal behavior of the 225 and 335 cm^{-1} modes was also measured at liquid-nitrogen temperature.

III. EXPERIMENTAL RESULTS

Figure 2 displays typical anti-Stokes Raman spectra over the 150 to 900 cm^{-1} spectral region for two pump-probe delay times in the $P_{\mathrm{pump}} \| c$, $P_{\mathrm{probe}} \| b$, and $P_{\mathrm{scatt}} \| b$ axis of the crystal scattering configuration. The thick-line spectrum was recorded at 1 ps pump-probe delay time, while the thin-line spectrum was obtained at 6 ps delay time. The intensities of the 225 and 335 cm^{-1} Raman lines exhibit delay-time-dependent changes with respect to the intensity of the rest of the spectral profile. This is demonstrated in Fig. 2 where we clearly see that the intensities of these two modes are stronger at 6 ps delay time, while the rest of the spectrum remains unchanged. ΔI denotes the difference in the intensity of the 225 and 335 cm^{-1} lines at delay times of 1 and 6 ps. The spectrum contains six distinct lines from which the 370 and 588 cm^{-1} lines are due to the pump beam, while the 225, 335, 545, and 826 cm^{-1} lines are due to the probe beam. The 370 cm^{-1} line is due to the pump beam and therefore, its intensity is independent from the pump-

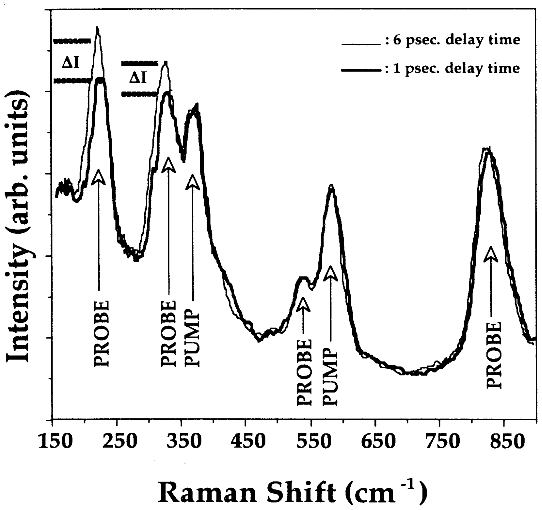

FIG. 2. Anti-Stokes Raman spectra for $\Delta\tau = 1$ ps (thick line) and $\Delta\tau = 6$ ps (thin line) delay times. Each spectrum contains Raman lines arising from the pump and the probe beams. ΔI denotes the increase in intensity of the 225 and 335 cm^{-1} Raman lines of the probe beam at $\Delta\tau = 6$ ps. The scattering configuration is $P_{\text{pump}} \| c$, $P_{\text{probe}} \| b$, and $P_{\text{scatt}} \| b$ axis of the crystal.

probe delay time for positive delay times. On the other hand, the 225 and 335 cm^{-1} anti-Stokes Raman lines which exhibit changes in intensity arise from the probe beam. The increase and subsequent decrease of the intensity of the 225 and 335 cm^{-1} modes is attributed to the generation of nonequilibrium phonons of the 225 and 335 cm^{-1} modes following the photoexcitation of the Cr ions by the pump pulse. The additional anti-Stokes Raman scattering signal arising from the nonequilibrium phonons is observed in only these modes that participate in the nonradiative relaxation. Figure 2 demonstrates that by monitoring the change in intensity of the 225 and 335 cm^{-1} anti-Stokes Raman lines at various delays between the pump and probe laser pulses we can obtain a picture of the dynamics of the corresponding nonequilibrium phonon populations.

Figure 3 displays the experimental data of the ratio of the intensities of the 225 and 335 cm^{-1} Raman lines over the intensity of the 370 cm^{-1} reference Raman line as a function of the pump-probe delay time. The 225 cm^{-1} mode profile reaches its maximum intensity in 10±1.5 ps and decays with time constant of 13.8±3 ps. The 335 cm^{-1} mode profile peaks at 8±1 ps and has a decay time of 10.3±3 ps. The temporal behavior of the change intensity of the 225 and 335 cm^{-1} anti-Stokes Raman lines depicts the dynamics of the nonequilibrium phonons on these two modes that are involved in the nonradiative decay of the Cr ions in forsterite.

The experiment was also performed with the sample held at liquid-nitrogen temperature. At this low temperature, no Raman lines due to the pump beam were observed because the thermal population of these modes (370 cm^{-1} or higher) is very small. The absence of a reference line to counterbalance the fluctuation of the laser beam power on the sample during the course of the experiment resulted in an enhanced experimental error in our measurements. An additional problem was the stronger noise level due to backscattering from more optical elements in the scattered light collection path and the modified microscope objective. Data shown in Fig. 4 represent the integrated intensities of the 225 and 335 cm^{-1} lines at various pump-probe delay times when the sample was held at liquid-nitrogen temperature. Although there is a significant fluctuation of the experimental data, it is clear that maximum intensity is obtained at ≈20 ps delay time. On the other hand, at room temperature the maximum intensity occurs at ≈9 ps delay time. This indicates that the relaxation times at low temperature are longer compared to the relaxation at room temperature.

The search for other phonon modes participating in the nonradiative relaxation was expanded by performing the experiment for two additional pump-probe-scattered light polarization configurations with the sample held at room temperature. These configurations covered most of the Raman phonon modes observed in the backscattering geometry. The second configuration is $P_{\text{pump}} \| c$, $P_{\text{probe}} \| b$, and $P_{\text{scatt}} \| c$ axis of the crystal where the Raman lines due to the probe beam are at 370, 609, and 856 cm^{-1}. Spectra for two delay times (1 and 10 ps) are shown in Fig. 5 We see that the intensity of the 370 cm^{-1} line is different for the two delay times (denoted as ΔI). Using as reference line the overlapping 300 and 335 cm^{-1} modes arising from the pump beam, the time dependence of the ratio of the intensity of the 370 cm^{-1} anti-Stokes Raman

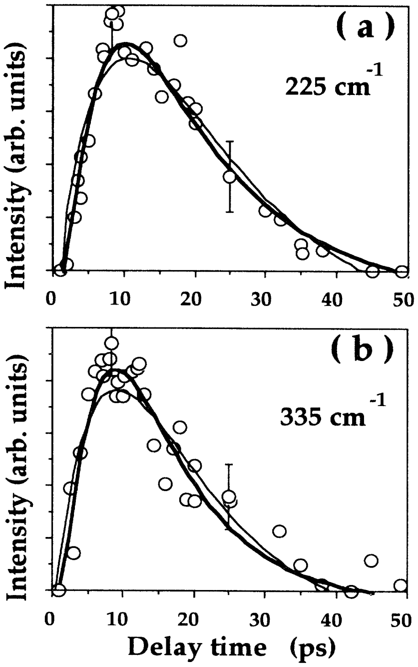

FIG. 3. Temporal behavior of the intensity of (a) the 225 cm^{-1} and (b) the 335 cm^{-1} phonon modes as a function of pump-probe delay time. The thick line represents the best fit when an initially populated intermediate state (bottleneck) is taken into account. The thin line is the best fit without the assumption of the intermediate state.

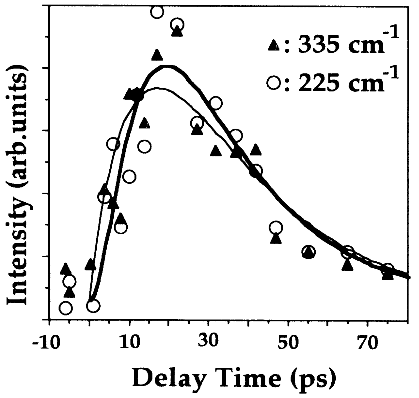

FIG. 4. The intensity of the 225 cm^{-1} (circles) and 335 cm^{-1} (triangles) anti-Stokes Raman lines as a function of the delay time at liquid-nitrogen temperature. The thick line curve represents fit of the experimental data obtained assuming the presence of the intermediate state ($t_d=5$ ps) and $t_{\text{phonon}}=22$ ps. The thin line is the fit when no intermediate state is taken into account ($t_d=0$) and using $t_{\text{phonon}}=20$ ps.

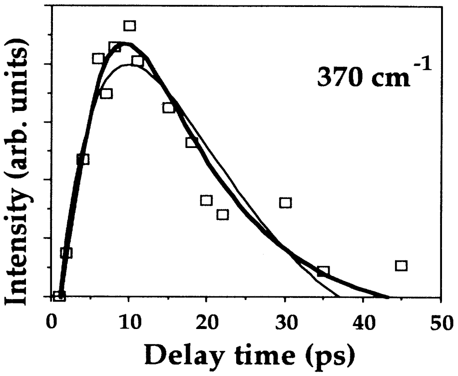

FIG. 6. Temporal behavior of the intensity of the 370 cm^{-1} phonon mode as a function of pump-probe delay time. The fitting curves were obtained by using the rate equations (1) and (3) and (a) taking into consideration the 2.1 eV electronic bottleneck (thick line) and (b) using $t_d=0$ (thin line).

line over the intensity of the reference Raman lines was measured. The experimental data of the intensity ratio of the 370 cm^{-1} line are shown in Fig. 6. The maximum intensity is observed at 9±1.5 ps and the population decays in 12.2±3.4 ps.

The third scattering configuration is $P_{\text{pump}}\|c$, $P_{\text{probe}}\|a$, and $P_{\text{scatt}}\|a$ axis. The probe-beam Raman lines to be examined are due to the 300, 502, 609, 770, 826, and 856 cm^{-1} modes. These modes are lattice modes of the Mg_2SiO_4 host crystal having A_g symmetry[13,14] except for the 502 and 770 cm^{-1} modes which are not mentioned in the literature as lattice modes. The 502 and 770 cm^{-1} modes that are clearly observed in the Cr^{4+}-doped forsterite crystal are not observed when the undoped or a Cr^{3+}-doped forsterite crystals are used. To understand the nature of these two modes, the following experiment was performed. Using the probe-beam scattering geometry ($P_{\text{probe}}\|a$, and $P_{\text{scatt}}\|a$ axis), anti-Stokes Raman spectra were obtained for various laser wavelengths. Figure 7 shows traces of anti-Stokes Raman spectra for 532, 575, 590, 609, 617, and 632 nm excitation wavelengths. The Raman lines at 856, 826, 609, and 424 cm^{-1} are lat-

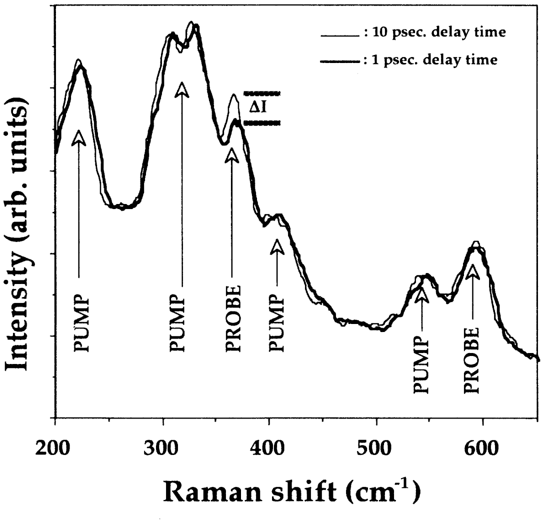

FIG. 5. Anti-Stokes Raman spectrum at 1 ps (thick line) and 10 ps (thin line) pump-probe delay times in the $P_{\text{pump}}\|c$, $P_{\text{probe}}\|b$, and $P_{\text{scatt}}\|c$ axis scattering configuration ΔI denotes the change in intensity of the 370 cm^{-1} probe-beam Raman line at 1 and 10 ps delay times.

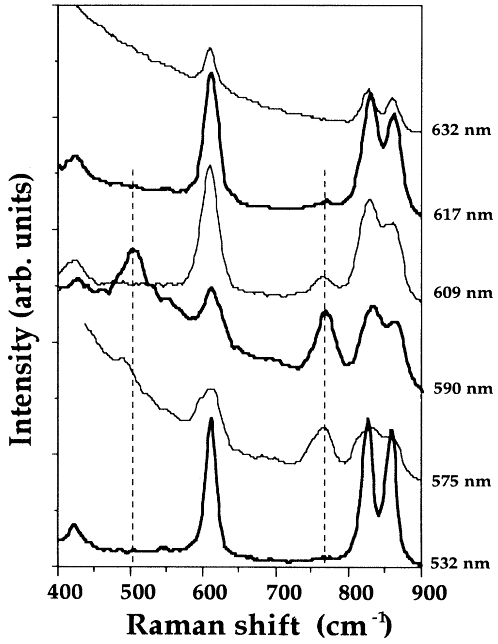

FIG. 7. Anti-Stokes Raman spectra under different laser excitation wavelengths. The two local modes shown with dashed line are located at 502 and 770 cm^{-1}. The laser polarization is $E\|a$ and the scattered light polarization is $P\|a$ axis.

tice modes and are observed in all spectra. In addition to the lattice modes, the two peaks at 502 and 770 cm^{-1} (marked with dashed lines) were observed only for certain excitation wavelengths. Apparently what we see is resonantly enhanced Raman scattering from local modes of the Cr^{4+} impurity ions in forsterite. The resonant enhancement of the anti-Stokes Raman lines of the local Cr^{4+}-ion modes occurs when the scattered photon is at resonance with the absorption band (for $E \| a$ axis in this case). Similar resonant behavior has been reported in semiconductors.[15]

Figure 8 displays anti-Stokes Raman spectra for three pump-probe delay times using the third configuration ($P_{\mathrm{pump}} \| c$, $P_{\mathrm{probe}} \| a$, and $P_{\mathrm{scatt}} \| a$ axis) in which the 502 and 770 cm^{-1} local modes are part of the probe-beam spectrum. In this arrangement we could not observe any detectable changes in the intensity of the probe-beam anti-Stokes Raman lines. The two Cr^{4+}-ion associated Raman lines do not exhibit any detectable change in intensity. Figure 8(a) demonstrates that the two modes do not show increase in intensity in the 1 ps time scale that it could be the case if the Cr^{4+}-ion local modes have a faster rise time due to their direct coupling with the Cr^{4+} ions. On the other hand, Fig. 8(b) shows that there is no detectable change in the 10 ps time scale (as we have seen with the 225, 335, and 370 cm^{-1} modes). These measurements indicate that neither the Cr^{4+}-ion modes (502 and 770 cm^{-1}) nor the rest of the lattice modes arising from the probe beam in this configuration (300, 605, 826, and 856 cm^{-1}) are involved in the energy transfer from the Cr ions into the lattice at least to the degree that the 225, 335, and 370 cm^{-1} phonon modes participate.

The time-resolved measurements presented above show the participation of the 225, 335, and 370 cm^{-1} phonon modes in the nonradiative relaxation of forsterite. The increased anti-Stokes Raman signal is due to the presence of an excess phonon population on these modes in addition to the thermal phonons. Subtracting the Raman profiles recorded at two delay times where the maximum and minimum intensities are observed, we can effectively obtain the anti-Stokes Raman spectrum of the nonequilibrium phonon populations. The resulted spectral profiles are shown in Fig. 9. More specifically, Fig. 9(a) was obtained by subtracting the anti-Stokes Raman spectra at 6 and 1 ps delay time in the $P_{\mathrm{pump}} \| c$, $P_{\mathrm{probe}} \| b$, and $P_{\mathrm{scatt}} \| b$ axis configuration. The peaks centered at ≈ 218 and

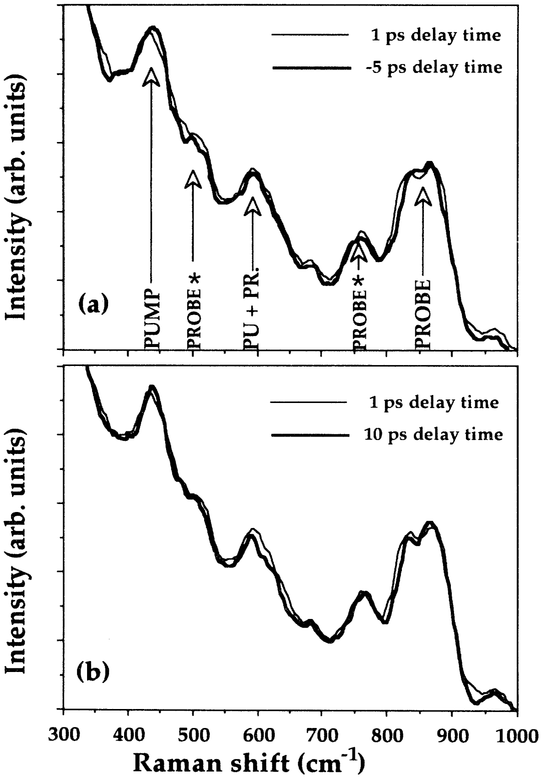

FIG. 8. Anti-Stokes Raman spectra at (a) 5 psec (thick line) and 1 psec (thin line) pump-probe delay times and (b) 10 psec (thick line) and 1 psec (thin line) pump-probe delay times in the $P_{\mathrm{pump}} \| c$, $P_{\mathrm{probe}} \| a$, and $P_{\mathrm{scatt}} \| a$ crystal axis scattering configuration. The two Raman lines associated with the Cr^{4+}-ion local modes are shown with an asterisk.

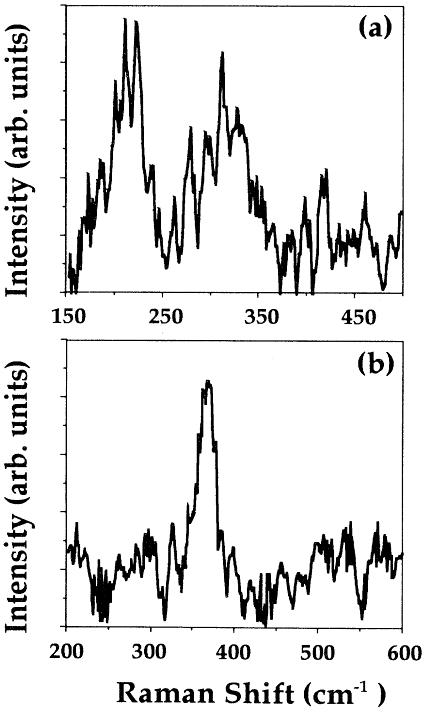

FIG. 9. The difference spectra obtained after subtraction of (a) the 1 ps delay-time anti-Stokes Raman spectrum from the 6 ps spectrum in the $P_{\mathrm{pump}} \| c$, $P_{\mathrm{probe}} \| b$, and $P_{\mathrm{scatt}} \| b$ axis and (b) the 1 ps from the 10 ps delay-time spectrum in the $P_{\mathrm{pump}} \| c$, $P_{\mathrm{probe}} \| b$, and $P_{\mathrm{scatt}} \| c$ axis scattering configuration. The peaks at ≈ 218 and ≈ 330 cm^{-1} in the first case and at ≈ 365 cm^{-1} in the second case indicate the presence of nonequilibrium phonon populations.

$\approx 330\ \text{cm}^{-1}$ are due to the increased intensity of the 225 and 335 cm^{-1} Raman lines at 6 ps delay time. Figure 9(b) was obtained by subtracting the anti-Stokes Raman spectra at 10 and 1 ps delay times in the $P_{\text{pump}}\|c$, $P_{\text{probe}}\|b$, and $P_{\text{scatt}}\|c$ axis configuration. The peak in this case is centered at $\approx 365\ \text{cm}^{-1}$ and is due to the increased intensity of the 370 cm^{-1} Raman lines at 10 ps pump-probe delay time. We see that the position of the lines on the effective nonequilibrium phonon Raman spectrum are located at frequencies slightly lower than the corresponding lattice modes.

IV. THEORETICAL APPROACH

The electron-lattice system dynamics is described using a rate equation model. The 590 nm laser light excites the Cr ions to the ${}^3T_1$ electronic state, 2.1 eV above the ground state. Immediately after photoexcitation, the excited ions are reaching an intermediate state which has a very short lifetime (t_d). This assumption is made in order to approximate the presence of the electronic bottleneck at 2.1 ± 0.15 eV shown in the up-converted hot luminescence spectra[9] which is directly populated by the 2.1 eV photons of the laser pulse. Assuming $t_d=0$, we can omit the presence of the intermediate state in our calculations. This intermediate state delays the nonradiative relaxation acting as sink of the available energy of the excited ions. The energy contained in the intermediate state $[E_d \sim I_{\text{pump}}\exp(-t/t_d)]$ is released by the excited ions following its depopulation and becomes the source of energy for the ionic system (E_e). Shortly afterwards the energy is transferred into the lattice system at a rate k (nonradiative relaxation rate) through the emission of phonons. Consequently, the rate equation describing the ionic system becomes

$$\frac{dE_e}{dt} = -kE_e + \frac{dE_d}{dt} \ . \tag{1}$$

Each vibrational mode (q_i) participating in the nonradiative relaxation absorbs energy from the electronic system at a rate k_i and decays at a rate λ_i due to is finite lifetime. The nonradiative relaxation rate (k) of the ionic system is the sum of the rates (k_i) for energy transfer to the different participating phonon modes ($k=\sum k_i$). The rate equation describing the total energy contained in a participating phonon mode $[E(q_i)]$ supplied by the nonradiatively relaxing ions can be written as

$$\frac{dE(q_i)}{dt} = k_i E_e - \lambda_i E(q_i) \ . \tag{2}$$

Rethermalization of the ion due to the generation of nonequilibrium phonon populations is not taken into account because the dominant effect in this time domain is the transfer of energy from the hot ions into the cold lattice environment, while the excess electronic energy to be transferred into the lattice is much bigger than the energy of the phonons emitted. In this analysis, the energy exchanged between the zero k-vector nonequilibrium phonons monitored in the time-resolved Raman experiment and phonons of other modes or within the same mode but different k vector will affect only the estimated phonon lifetime.

The rate equation describing the nonequilibrium phonon population $[\Delta n(q_i)]$ is obtained using Eq. (2) and the relation $E(q_i)=\Delta n(q_i)\hbar\omega_i$:

$$\frac{d\Delta n(q_i)}{dt} = \frac{k_i E_e}{\hbar\omega_i} - \lambda_i \Delta n(q_i) \ . \tag{3}$$

Equation (3) describes the generation of nonequilibrium phonons of a mode (q_i) due to the transfer of energy from the ion into this mode at a rate (k_i) followed by the destruction of these phonons due to their finite lifetime (λ_i^{-1}).

The intensity of the anti-Stokes Raman lines due to the probe beam $[I_{\text{AS}}(q_i,\Delta\tau)]$ as function of the delay time $\Delta\tau$ is proportional to the average phonon population $[n(q_i)]$ of this mode:

$$I_{\text{AS}}(q_i,\Delta\tau) \sim n(q_i,\Delta\tau) = n_{\text{th}}(q_i) + \Delta n(q_i,\Delta\tau) \ , \tag{4}$$

where $n_{\text{th}}(q_i)$ is the lattice phonons population under thermal equilibrium and $\Delta n(q_i,\Delta\tau)$ is the nonequilibrium phonon population generated by the pump pulse. The change in intensity of a probe beam associated Raman line $[\Delta I_{\text{AS}}(q_i,\Delta\tau)]$ is linearly related to the generated nonequilibrium phonon population:

$$\Delta I_{\text{AS}}(q_i,\Delta\tau) \sim \Delta n(q_i,\Delta\tau) \ . \tag{5}$$

The above relationships show that by monitoring the changes of the intensity of the anti-Stokes Raman line the temporal evolution of the nonequilibrium phonon populations is obtained. The nonradiative relaxation parameters can be estimated from the change in intensity of the probe-beam anti-Stokes Raman lines.

In our analysis, employing nonlinear least-squares fitting of Eqs. (1) and (3) using the Simplex method[16] to the experimental data we estimate the nonradiative relaxation parameters of the system. The shape of the curves is determined by the nonradiative relaxation rate k, the intermediate state lifetime t_d, and the phonon lifetime $t_{\text{phonon}}=\lambda_i^{-1}$. The first two ($k$ and t_d) should be the same for all participating modes since they describe the relaxation of the ionic system and therefore, the phonon lifetime is the only independent parameter. For simplicity in the estimation of the relaxation parameters and considering that the measured time-dependent changes are in the 10 ps time scale, while the laser pulse width is of the order of 100 fs, we have assumed square laser pulses.

Fitting of the experimental data for the 225 and 335 cm^{-1} modes at room temperature is displayed in Fig. 3. Curves from this model shown in Figs. 3(a) and 3(b) with a thick line describe the data points very well. The estimated relaxation parameters are $t_d=3\pm1.6$ ps lifetime for the initially populated intermediate state, $k^{-1}=2.8\pm1.6$ ps for the nonradiative relaxation time, and the phonon lifetimes are $\lambda_{225}^{-1}=15.7\pm2.8$ ps and $\lambda_{335}^{-1}=10.4\pm2.8$ ps for the 225 and 335 cm^{-1} modes, respectively. When no intermediate state is taken into account ($t_d=0$), the parameters for the fit [shown in Figs. 3(a) and 3(b) with thin line] are $k^{-1}=8.5\pm1.6$ ps for the nonradiative relaxation time, while the phonon lifetimes are $\lambda_{225}^{-1}=13.7\pm2.8$ ps and $\lambda_{335}^{-1}=9.7\pm2.8$ ps.

The experimental data with the sample held at liquid-nitrogen temperature indicate a slower nonradiative relaxation. The fitting shown in Fig. 4 with thick line was obtained using Eqs. (1) and (3). The fitting parameters are $t_d=5\pm3.1$ ps lifetime for the initially populated intermediate state, $k^{-1}=8\pm3.1$ ps for the nonradiative relaxation time and the phonon lifetimes are $\lambda_{225}^{-1}=22.3\pm4.9$ ps and $\lambda_{335}^{-1}=21.8\pm4.9$ ps. The thin line in Fig. 4 represents the best fitting using the approximation that does not include the presence of the intermediate state ($t_d=0$). In this case, the relaxation parameters are $k^{-1}=15\pm2.9$ ps, $\lambda_{225}^{-1}=20.2\pm4.6$ ps, and $\lambda_{335}^{-1}=19.8\pm4.6$ ps. Due to the fluctuation of the data the experimental error on the estimated parameters is large. However, there is no question that all relaxation parameters are longer at low temperatures.

Figure 6 shows best fitting of the experimentally measured change in intensity of the 370 cm^{-1} Raman line as a function of the delay time. Using Eqs. (1) and (3), best fit is shown with thick line where the estimated intermediate state lifetime is $t_d=3\pm1.7$ ps, the nonradiative relaxation item $k^{-1}=2.8\pm1.7$ ps and the phonon mode lifetime $\lambda_{370}^{-1}=12.1\pm3.1$ ps. Using the dual relaxation model ($t_d=0$, thin-line curve), the estimated nonradiative relaxation time $k^{-1}=8.5\pm1.8$ ps and the phonon lifetime $\lambda_{370}^{-1}=11.6\pm3.2$ ps.

TABLE II. The nonradiative relaxation parameters estimated using the rate equations (1) and (3) and the experimental data of the intensity ratio of the 225, 335, and 370 cm^{-1} anti-Stokes phonon lines. t_d: lifetime of the initially populated intermediate state (bottleneck at 2.1 eV), k^{-1}: nonradiative relaxation time of the electronic system (k: rate for energy transfer from the ion into the lattice), t_{phonon}: lifetime of the nonequilibrium phonons (λ_i^{-1}).

Phonon mode / Temperature	Estimated relaxation parameters assuming the 2.1 eV bottleneck (intermediate state)	Estimated relaxation parameters assuming no intermediate state at 2.1 eV
225 cm^{-1} / T=293 K	t_d = 3 ± 1.6 ps k^{-1} = 2.8 ± 1.6 ps t_{phonon} = 15.7 ± 2.8 ps	t_d = 0 k^{-1} = 8.5 ± 1.6 ps t_{phonon} = 13.7 ± 2.8 ps
225 cm^{-1} / T=80 K	t_d = 5 ± 3.1 ps k^{-1} = 8 ± 3.1 ps t_{phonon} = 22.3 ± 4.9 ps	t_d = 0 k^{-1} = 15 ± 2.9 ps t_{phonon} = 20.2 ± 4.6 ps
335 cm^{-1} / T=293 K	t_d = 3 ± 1.6 ps k^{-1} = 2.8 ± 1.6 ps t_{phonon} = 10.4 ± 2.8 ps	t_d = 0 k^{-1} = 8.5 ± 1.6 ps t_{phonon} = 9.7 ± 2.8 ps
335 cm^{-1} / T=80 K	t_d = 5 ± 3.1 ps k^{-1} = 8 ± 3.1 ps t_{phonon} = 21.8 ± 4.9 ps	t_d = 0 k^{-1} = 15 ± 2.9 ps t_{phonon} = 19.8 ± 4.6 ps
370 cm^{-1} / T=293 K	t_d = 3 ± 1.6 ps k^{-1} = 2.8 ± 1.6 ps t_{phonon} = 12.1 ± 3.1 ps	t_d = 0 k^{-1} = 8.5 ± 1.6 ps t_{phonon} = 11.6 ± 3.2 ps

The estimated relaxation parameters for the three modes participating in the nonradiative relaxation are summarized in Table II. From the fitting to the experimental data using the rate equations (1) and (3) it appears that the best fitting is obtained using the model that includes the presence of the electronic bottleneck immediately after excitation (thick-line fitting curves in Figs. 3, 4, and 6). To verify that the adaptation of the intermediate state in our model improves the fitting of the experimental data we estimated for each participating phonon mode the ratio (R) of the sums of the squares (residuals) using the model which includes the intermediate state ($t_d\neq0$) over the sums of the squares using the dual relaxation model ($t_d=0$). We estimated that this ratio for the 225, 335, and 370 cm^{-1} modes at room temperature is $R_{225}=0.46$, $R_{335}=0.44$, and $R_{370}=0.61$, respectively. For the measurements performed at low temperature we estimated $R_{225}=0.78$ and $R_{335}=0.73$ for the 225 and 335 cm^{-1} modes, respectively. This clearly shows that the model which includes the intermediate state provides a better fitting of the experimental data.

In the $t_d=0$ approximation, the data points in the early part of the temporal profile are below the fitting curve, while in the maximum intensity position the data points are above the curve. We could have achieved a better fitting of the experimental data using the simple dual relaxation model ($t_d=0$) by shifting the "zero" delay time by ≈2 ps. This shift is unrealistic since our zero delay time is known to within ±150 fs. This suggests that the model we have used assuming the intermediate state just below the excitation level that delays the nonradiative relaxation by few ps is closer to the reality. Another possibility is that the observed modes do not participate in the early part of the nonradiative relaxation due to different selection rules at different parts of the electronic excited state. This later mechanism is unlikely because all the observed participating modes require the same shift of the "zero" delay time in order to achieve best fitting using the $t_d=0$ approximation.

V. DISCUSSION

The lasing ion in forsterite is the tetravalant chromium.[11,12] The Cr^{4+} ions replace Si in the Mg_2SiO_4 host in tetrahedrally coordinated sites. The 225 cm^{-1} mode is a translational mode of the $-SiO_4$ tetrahedral. The 335 cm^{-1} mode arises from two phonon modes ≈10 cm^{-1} apart which are spectrally overlapping due to the wide spectral width of our laser; one mode is a rotational mode of the $-SiO_4$ tetrahedron at 330 cm^{-1}, while the other is a translational mode of Mg ions located at 340 cm^{-1}. Both modes have A_g symmetry.[13,14] The 370 cm^{-1} mode is a rotational mode of the $-SiO_4$ tetrahedron having B_{2g} symmetry. On the other hand, the remaining of the investigated lattice phonon modes (300, 545, 590, 609, 826, 856, and 884 cm^{-1}) that do not exhibit delay time-dependent changes are of A_g or B_{2g} symmetry. This suggests that symmetry is not the only important factor on which phonon modes participate in the nonradiative decay.

In the difference spectra shown in Fig. 9, the peaks are slightly shifted with respect to peaks observed in the anti-Stokes Raman spectrum. More specifically, in Fig. 9(a) the peaks are located at ≈ 218 and ≈ 330 cm^{-1} instead of 225 and 335 cm^{-1}, respectively. In Fig. 9(b) the peak in the difference spectrum is at ≈ 365 cm^{-1} instead of 370 cm^{-1}. This displacement of the nonequilibrium phonon modes towards lower frequencies can be explained. The Cr^{4+} ions are heavier than the Si ions that they substitute in forsterite. The vibration of the lattice involving the heavier impurity center causes a lower vibrational frequency than the equivalent pure lattice vibrations. The phonons generated during the nonradiative relaxation are coupled with the Cr ions and as a result, their frequency is lowered with respect to the pure lattice modes.

The estimated phonon lifetimes of the 225 and 335 cm^{-1} phonon modes show that at liquid nitrogen the lifetime of the generated phonons is longer than at room temperature. The optical phonons are splitting into lower energy phonons due to the anharmonic interactions within the lattice. Theoretical considerations,[17] Raman phonon mode linewidth measurements,[18,19] and time-resolved experiments[20,21] have shown that the phonon lifetimes are longer at lower temperatures which is in agreement with our experimental observations. The estimated nonradiative relaxation time (k^{-1}) at 78 K is longer than the relaxation time at room temperature. The lower relaxation rates at decreased temperatures is a common characteristic of the nonradiative relaxation process.[22,23] Unfortunately, the experimental error in our estimated relaxation parameters does not allow for further trustworthy analysis of these results based on the theoretical approach of the nonradiative relaxation and the anharmonic decay of the optical phonons.

The intensity of the 225 and 335 cm^{-1} anti-Stokes Raman lines at various delay times were simultaneously monitored using the same scattering configuration (see Fig. 2). The relative increase of their anti-Stokes Raman signal is proportional to the relative increase of their effective phonon occupation number $\Delta n(q_i)$. The intensity ratio of a Raman line at the maximum and minimum position of the temporal profile can be written as

$$\frac{I(q_i)_{\max}}{I(q_i)_{\min}} \approx \frac{n_{\text{th}}(q_i)+\Delta n(q_i)}{n_{\text{th}}(q_i)}$$

or

$$\Delta n(q_i) \approx n_{\text{th}}(q_i)\frac{I(q_i)_{\max}-I(q_i)_{\min}}{I(q_i)_{\min}} , \tag{6}$$

where $n_{\text{th}}(q_i)$ is the thermal phonon occupation number of the (q_i) mode at room temperature, while $I(q_i)_{\max}$ and $I(q_i)_{\min}$ are the maximum and minimum intensities of the anti-Stokes Raman line of the probe beam. Using Eq. (6) and the experimentally measured maximum and minimum intensity of the 225 and 335 cm^{-1} lines leads to an approximate value of the ratio of energy transferred to these two modes:

$$\frac{\Delta n(225)}{\Delta n(335)} \approx 2.4 \tag{7a}$$

or

$$\frac{h\omega_{225}\Delta n(225)}{h\omega_{335}\Delta n(335)} \approx 1.6 . \tag{7b}$$

Equation (7a) provides the ratio of the phonons emitted from each mode, while Eq. (7b) is the ratio of the energies transferred into these two modes. It follows that the relation between the energy transfer rates from the electronic system into the 225 and 335 cm^{-1} modes is approximately $k_{225} \approx 1.6 k_{335}$. This method cannot be used for the case of the 370 cm^{-1} mode because the pump over the probe-beam power was 1/1 instead of 1/3 used for the 225 and 335 cm^{-1} modes. However, the change of the intensity of the 370 cm^{-1} mode is slightly smaller than the change of the 335 cm^{-1} mode. If we take into account that the pump beam is more intense in the case of the 370 cm^{-1} mode and that the same $\Delta N(q)$ for both modes causes a larger increase in the intensity of the 370 cm^{-1} mode (due to the smaller thermal occupation number), we can conclude that the 370 cm^{-1} phonons emitted are at most as many as the 335 cm^{-1} phonons [$\Delta n(370) \le \Delta n(335)$]. All the above discussion is valid under the condition that the resonant enhancement of the anti-Stokes signal from the nonequilibrium phonons is the same for all these modes.

The rate equations model allows for the estimation of the lifetime of the 2.1 eV electronic bottleneck. The estimated lifetimes are $t_d = 3\pm1.6$ ps and $t_d = 5\pm3.1$ ps at room and liquid-nitrogen temperatures, respectively. The nonradiative relaxation time (k^{-1}) represents the time that the electronic system needs to cross the region of the $^3T_1(t_2^2)$ excited state from the end of the bottleneck at $\approx 16\,150$ cm^{-1} to the bottom of the $^3T_1(t_2^2)$ state at $\approx 12\,850$ cm^{-1}. The lifetime of the $^3T_1(t_2^2)$ state is of the order of hundreds of nanoseconds.[23] The nonradiative relaxation from the $^3T_1(t_2^2)$ state towards the bottom of the $^3T_2$ state is in a different (100 ns) time scale and it does not affect the analysis of this experiment which is in the ps time scale. If we assume that only the 225, 335, and 370 cm^{-1} phonon modes are involved in the nonradiative relaxation and taking into account the previously estimated relations for the phonons emitted [$\Delta n(225)/\Delta n(335) \approx 2.4$ and $\Delta n(370) \le \Delta n(335)$], we deduce one possible division of the number of phonons for the available energy of 3300 cm^{-1} as distributed among seven (7) 225 cm^{-1} phonons, three (3) 335 cm^{-1} phonons and two (2) 370 cm^{-1} phonons for a total of 12 phonons emitted per photoexcited ion. At room temperature, the estimated nonradiative relaxation time is 2.8 ps which implies that the average time between phonon emission is ~230 fs (2.8 ps/12). At liquid-nitrogen temperature, the estimated nonradiative relaxation time is 8 ps which means that the average time between the emission of two phonons is ≈ 665 fs (8 ps/12). The later estimated value is identical with the estimated lifetime of the first vibronic level (660 fs) of the up-converted hot luminescence spectrum under 532 nm excitation.[24]

The phonon modes involved in the vibrational relaxation in forsterite as they were determined by the up-converted hot luminescence experiments[8,9] are 218±20, 325±20, 365±20, and 513±12 cm^{-1}. On the other hand, in the difference spectra obtained after subtraction of the

Raman spectra at different delay times, the nonequilibrium phonon peaks are located at ≈218, ≈330, and ≈365 cm^{-1}. We see that there is good agreement between the two experiments and only the 513 cm^{-1} mode was not indicated by the time resolved Raman experiments. The 513 cm^{-1} mode is only infrared active[14] (B_{2u} symmetry) and therefore, the participation of this mode was impossible to be determined with a time-resolved Raman experiment.

The rate equations utilized to describe the experimental data incorporate the assumption that an intermediate state was populated immediately after photoexcitation in order to approximate the presence of the electronic bottleneck at 2.1 eV. This assumption allows for an evaluation of the lifetime of the bottleneck which was estimated to be $t_d = 3 \pm 1.6$ ps and $t_d = 5 \pm 3.1$ ps at room and liquid-nitrogen temperatures, respectively. On the other hand, the lifetime of up-converted emission from the 2.1 eV bottleneck was determined to be shorted than 10 ps at room and liquid-nitrogen temperatures. Therefore, there is agreement between the two experimental techniques.

The present experimental investigation of the nonradiative relaxation in forsterite provides a clue on which are the selection criteria for the participating phonon modes. The time-resolved Raman experiments have shown that symmetry does not seem to play an important role. This means that we should concentrate our attention on another criterion. The other interesting observation is that all the participating phonon modes as they were determined by the up-converted hot luminescence measurements and in the difference spectra of the time-resolved Raman experiments (Fig. 9) have frequencies almost identical to lattice modes of forsterite. The local modes describe the vibrational state of the impurity ion immediately after excitation. It seems logical that the energy transfer from the excited into a high vibrational level impurity ion following the photoexcitation occurs through these lattice modes that have frequencies degenerate to the local vibrations of the impurity ion. It has been shown[25] that in binary liquids a normal vibrational mode of component A relaxes via energy transfer to a normal mode of component B when resonance occurs. This behavior is similar to our experimental observation which suggests that the energy transfer from the excited impurity ions into the lattice occurs through the lattice modes that are in resonance with the local vibrations of the excited ions.

The dynamics of the 225, 335, and 370 cm^{-1} phonon modes was time resolved at room and liquid-nitrogen temperatures. The modes exhibited time-dependent changes while in a number of other modes we have not detected any changes. The low-temperature relaxation parameters are significantly longer than at room temperature. In our fitting model we included the presence of the bottleneck at 2.1 eV. This addition significantly improved the fitting of the experimental data and provides an estimation of the lifetime of the bottleneck.

ACKNOWLEDGMENTS

This research is supported by the Army Research Office. We thank Bob Guenther for helpful discussions.

---

[1] S. K. Gayen, W. B. Wang, V. Petričević, R. Dorsinville, and R. R. Alfano, Appl. Phys. Lett. **47**, 455 (1985).

[2] S. K. Gayen, W. B. Wang, V. Petričević, and R. R. Alfano, Appl. Phys. Lett. **49**, 437 (1986).

[3] S. K. Gayen, W. B. Wang, V. Petričević, S. G. Demos, and R. R. Alfano, J. Lumin. **47**, 181 (1991).

[4] B. Henderson and G. F. Imbusch, *Optical Spectroscopy of Inorganic Solids* (Wiley, New York, 1989), Chap. 5 and 9.

[5] M. J. Van Dort, C. R. de Kok, J. I. Dijkhuis, and H. W. de Wijn, J. Lumin. **45**, 150 (1990).

[6] D. M. Boye, J. E. Rives, and R. S. Meltzer, J. Lumin. **45**, 147 (1990).

[7] W. A. Tolbert, W. M. Dennis, and W. M. Yen, Phys. Rev. Lett. **65**, 607 (1990).

[8] S. G. Demos and R. R. Alfano, Phys. Rev. B **46**, 8811 (1992).

[9] S. G. Demos, Y. Takiguchi, and R. R. Alfano, Opt. Lett. **18**, 522 (1993).

[10] S. G. Demos, J. M. Buchert, and R. R. Alfano, Appl. Phys. Lett. **61**, 660 (1992).

[11] V. Petričević, S. K. Gayen, R. R. Alfano, K. Yamagishi, H. Anzai, and Y. Yamaguchi, Appl. Phys. Lett. **52**, 1040 (1988); **53**, 2590 (1988).

[12] Weiyi Jia, Huimin Liu, S. Jaffe, B. Denker, and W. M. Yen, Phys. Rev. B **43**, 5234 (1991).

[13] V. Devarajan and E. Funck, J. Chem. Phys. **62**, 3406 (1975).

[14] Kazuaki Iishi, Am. Mineral. **63**, 1198 (1978).

[15] J. Shah, A. E. DiGiovanni, T. C. Damen, and B. I. Miller, Phys. Rev. B **7**, 3481 (1973).

[16] J. A. Nedler and R. Mead, Comput. J. **7**, 308 (1965); Marco S. Caceci and William P. Cacheris I, Byte **19**, 340 (1994).

[17] P. G. Klemens, Phys. Rev. **148**, 845 (1966).

[18] K. Park, Phys. Lett. **22**, 39 (1966).

[19] B. Kh. Bairamov, Yu. E. Kitaev, V. K. Negoduiko, and Z. M. Khashkhozhev, Sov. Phys. Solid State **16**, 1323 (1975).

[20] A. Laubereau, D. von der Linde, and W. Kaiser, Phys. Rev. Lett. **27**, 802 (1971).

[21] J. A. Kash, J. C. Tsang, and J. M. Hvam, Phys. Rev. Lett. **54**, 2151 (1985).

[22] L. A. Riseberg and H. W. Moos, Phys. Rev. **174**, 429 (1968).

[23] J. M. Wisenfeld, Linn F. Mollenauer, and Erich Ippen, Phys. Rev. Lett. **47**, 1668 (1981).

[24] S. G. Demos, V. Petričević, and R. R. Alfano, Phys. Rev. B (to be published).

[25] A. Laubereau, L. Kirschner, and W. Kaiser, Opt. Commun. **9**, 182 (1973).